Aeroelastic Deformation Effects on the Stopped-Rotor Dynamics of an X-Wing Aircraft

Michael G. Gilbert*
NASA Langley Research Center, Hampton, Virginia
and
Walter A. Silva†
Planning Research Corporation, Hampton, Virginia

A new design concept in the development of vertical takeoff and landing aircraft with high forward flight speed capability is that of the X-wing. The X-wing is a stiff, bearingless helicopter rotor system that can be stopped in flight and the blades used as two forward-swept wings and two aft-swept wings. Because of the unusual configuration in the fixed-wing mode, there is a high potential for aeroelastic divergence or flutter and coupling of blade vibration modes with rigid-body modes. An aeroelastic stability analysis of an X-wing configuration aircraft was undertaken to determine whether these problems were likely. This paper reports on the results of dynamic stability analysis in the lateral and longitudinal directions, including the vehicle rigid-body and flexible modes. A static aeroelastic analysis using the normal vibration mode equations of motion was performed to determine the cause of a loss of longitudinal static margin with increasing airspeed. This loss of static margin was found to be due to aeroelastic wash in of the forward-swept blades and wash out of the aft-swept blades moving the aircraft aerodynamic center forward of the center of gravity. This phenomenon is likely to be generic to X-wing aircraft.

Introduction

In recent years, there has been new interest in the development of vertical takeoff and landing (VTOL) aircraft that are capable of high-speed forward flight. Two concepts currently under consideration are the tilt-rotor and X-wing aircraft designs. Both concepts promise to deliver an aircraft with helicopter-like hover, takeoff, and landing capability with high subsonic forward flight speeds comparable to current turboprop aircraft. In the tilt-rotor design, tandem rotors are mechanically rotated between the vertical and horizontal positions for various phases of the flight. In the X-wing concept, the rotating rotor system is stopped in flight and used as fixed wings for forward flight.

The X-wing rotor is a stiff, bearingless, four-blade helicopter rotor system that uses circulation-control aerodynamic blowing to maintain and control lift on the blades and provide cyclic, collective, and higher-harmonic control inputs. The system incorporates a mechanical brake that is used to stop the rotary motion and lock the blades into position as two forward-swept and two aft-swept wings for the high-speed portions of the flight, with circulation-control blowing again used to control lift and provide fixed-wing flight control inputs.

The X-wing rotor blades each have an elliptical cross section and full-span blowing slots located near the fore and aft edges. High-pressure air is blown from the trailing-edge slot in both the rotary and fixed-wing flight modes to provide direct lift augmentation of each blade that is independent of the blade angle of attack. The high-pressure blowing stream re-energizes the separated flows typical in the trailing-edge region, causing the separated flow to reattach to the airfoil. This reattachment pushes the trailing-edge stagnation point aft, increases the airfoil circulation and, therefore, increases the airfoil lift. For a typical circulation-control blown airfoil, as the amount of blowing is increased, the lift of the airfoil is increased, but the airfoil blowing stall angle is decreased. The blowing stall angle refers to the angle of attack at which the lift-curve slope of the blown airfoil becomes negative, even though the airflow over the airfoil is still attached. The moment coefficient at half-chord for a typical circulation control blowing airfoil is for the most part unaffected by variations in the amount of blowing.

Haas and Chopra[1] recently studied the aeroelastic stability of a high-aspect-ratio, cantilevered wing with circulation-control blowing that was similar to an X-wing rotor blade. Two distinct flutter mechanisms were identified. The first mechanism involved the unswept wing with no blowing and consisted of a classical coalescence of two coupled modes at a high-speed condition. The second mechanism, termed "circulation-controlled flutter," consisted of a low-speed bending mode instability of an unswept wing at an angle of attack greater than the blown stall angle, i.e., where the lift-curve slope is negative. The same circulation-control airfoil at angles of attack less than the blown stall angle and the same amount of blowing did not encounter circulation-control flutter.

A flight-test program to demonstrate conversion of an X-wing rotor from rotary to fixed-wing and fixed-wing to rotary modes was initiated but was subsequently canceled. An X-wing rotor was built by the Sikorsky Aircraft Company to be flown on a modified Rotor Systems Research Aircraft (RSRA).[2] Northrop Aircraft Corporation assisted Sikorsky in the development of the fixed-wing flight control sytems and aeroelastic stability analyses.The RSRA/X-wing aircraft configuration is shown in Fig. 1.

The unusual configuration of an X-wing aircraft in the stopped-rotor or fixed-wing mode led to concern regarding aeroelastic stability and the potential for aeroelastic interactions with the flight control systems and flight dynamics of the

Presented as Paper 87-2563 at the AIAA Atmospheric Flight Mechanics Conference, Monterey, CA, Aug. 17-19, 1987; received Jan. 12, 1988; revision received Oct. 19, 1987.

*Aerospace Engineer, Aeroservoelasticity Branch, Structural Dynamics Division. Member AIAA.

†Structures Engineer, Aerospace Technologies Division. Member AIAA.

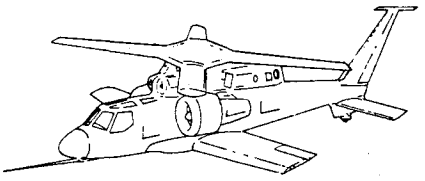

Fig. 1 RSRA/X-wing vehicle.

vehicle. As a result, detailed aeroservoelastic (ASE) analyses of the vehicle were planned, and the initial state-space models describing the vehicle aeroelastic characteristics for small to moderate amounts of circulation-control blowing were developed. The first section of this paper describes the development of the state-space models for the vehicle longitudinal and lateral dynamics, including the effects of rigid-body dynamics, flexible-vehicle deformations, unsteady aerodynamics, and deflected control surfaces. The following section gives the results of an analysis of the vehicle dynamics, including aeroelastic deformations. The third section presents the results of a static aeroelastic analysis of the vehicle for the longitudinal case. This analysis was undertaken because of an analytically predicted change in the aircraft short-period dynamics due to static structural deformation and was performed using the normal mode equations of motion of the flexible vehicle.

Equations of Motion

Stability analyses of flexible aircraft require the development of suitable mathematical models describing the vehicle flight dynamics, structural dynamics, aerodynamics, and control inputs. For the analysis described here, separate state-space mathematical models for the longitudinal and lateral dynamics of the X-wing vehicles were developed using the Interaction of Structures, Aerodynamics, and Controls (ISAC) computer programs.[3]

The models were developed to represent accurately the aeroelastic characteristics of the vehicle and include control surface deflections but do not include closed-loop flight control or stability augmentation systems, higher-harmonic control systems, or hub-moment-feedback systems. The dynamics associated with these systems would normally be added later as part of an ASE analysis. In addition, a linear aerodynamic theory was used for the model developments that does not explicitly include circulation-control blowing effects. The use of a linear aerodynamic theory is considered valid here under the following assumptions: 1) a small to moderate amount of circulation-control blowing is being used to maintain attached flow over the airfoil; and 2) the airfoil angle-of-atack variations are sufficiently small enough that the the stagnation point behaves as it would for a sharp trailing-edge airfoil, and the airfoil angle of attack is less than the airfoil blown stall angle. These assumptions limit the analysis to a region where circulation-control flutter is not a problem.

The equations of motion of a flexible, free-flying aircraft can be written in terms of vehicle rigid-body modes, vehicle structural vibration modes, and control surface deflection modes. For a finite number of modes n, the deformation of the vehicle is written as the product of mode shapes and time-dependent generalized coordinates as

$$d(t) = \Phi\eta(t) \tag{1}$$

where $d(t)$ is the m vector of vehicle displacements at various points on the vehicle, $\eta(t)$ is an n, $n<m$ vector of generalized coordinates, and the n columns of Φ are the mode shapes of the vehicle.

Using this modal representation of the vehicle, the equations of motion are[4]

$$[Ms^2 + Cs + K + qQ(s)]\xi + qQ_c(s)\delta = 0 \tag{2}$$

where s is the Laplace transform variable, ξ the generalized coordinate vector of the rigid-body and vibration modes, and δ the vector of generalized coordinates for the control surface deflection modes such that $\eta^T = \{\xi^T | \delta^T\}$. The M, C, and K are generalized mass, damping, and stiffness matrices, respectively, and q is the dynamic pressure. The matrices $Q(s)$ and $Q_c(s)$ are rational function approximations to tabulated unsteady generalized aerodynamic forces (GAF's) calculated for harmonic motion of the rigid-body, flexible, and control surface deflection modes. The approximation technique is described further in the following discussion.

For this study, vehicle mode shape data, calculated using a NASTRAN finite-element model of the RSRA/X-wing aircraft, were obtained from Northrop Aircraft Corporation. These data were separated into symmetric and antisymmetric modes for the longitudinal and lateral model developments. Table 1 lists the frequency and generalized masses of the rigid-body and elastic modes.

Unsteady GAF's, which are a function of reduced-frequency $k = \omega b/V$, where ω is the frequency of oscillation, b a reference length, and V the velocity, were calculated for harmonic motion in ISAC using doublet-lattice aerodynamics. The same aerodynamic paneling, which includes the X-wing rotor and RSRA lifting surfaces but not the RSRA fuselage, was used for both the longitudinal and lateral cases. Figure 2

Table 1 Vehicle modal data

Symmetric		Antisymmetric	
Frequency, Hz	Mass, lb-s^2/in.	Frequency, Hz	Mass, lb-s^3/in.
0.0	86.84	0.0	86.15
0.0	4.85	0.0	7.14
3.64	1.29	0.0	5.72
5.09	0.71	1.79	2.03
5.61	2.01	4.44	1.36
6.58	1.31	4.91	1.24
8.91	0.50	5.08	0.79
8.99	2.39	6.07	0.35
10.5	1.75	6.19	0.88
12.2	1.62	6.25	0.88
13.2	1.93	6.32	10.8
14.5	0.013	6.54	1.19
16.5	0.006	6.63	1.35
17.7	0.033	6.76	12.4
20.3	0.014	7.50	0.84
20.9	0.112	7.57	0.82
22.0	0.80	8.53	8.94
24.2	1.00	9.85	1.19
26.4	0.141	10.8	0.54
29.4	0.129	12.0	1.25

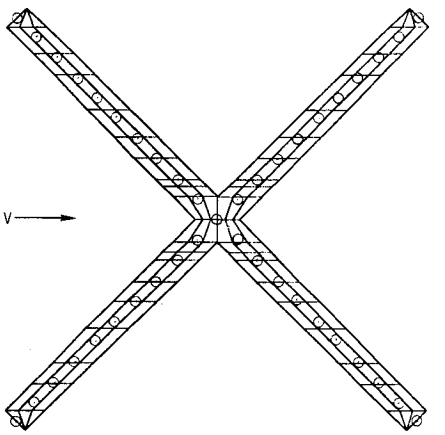

Fig. 2 X-Wing rotor aerodynamic paneling and structural node locations.

shows the aerodynamic panel layout of the X-wing rotor and the location of points at which vibration mode displacement data were available. A surface-spline routine within ISAC was used to calculate the displacements and slopes of each aerodynamic panel for every mode based on the mode shape displacements at the structural data points. The panel displacements and slopes are used in doublet lattice to calculate the unsteady GAF's.

The GAF's calculated by doublet lattice for harmonic motion are output as complex tabulated data at each k for a given Mach number. These forces must be extended to arbitrary motion (complex frequency $s=\sigma+j\omega$) for use in dynamic stability analyses. The extension to arbitrary motion is accomplished using a rational function approximation technique[5,6] as

$$[Q(s)\,|\,Q_c(s)] = A_0 + A_1\left(\frac{bs}{V}\right) + A_2\left(\frac{bs}{V}\right)^2 + \sum_{i=1}^{L}\frac{B_i s}{[s+(V/b)\beta_i]} \tag{3}$$

where β_i are aerodynamic lag coefficients and L is the number of lags. The real matrices A_j and B_i are determined by a least-squares fit to the real and imaginary parts of the tabulated unsteady aerodynamic forces at $s=j\omega$ for a given set of lags β_i, which are arbitrarily selected to be within the reduced-frequency range of interest. For the longitudinal and lateral model developments, four aerodynamic lags, $\beta_i=0.1$, 0.2, 0.35, 0.5, were used. In addition, constraints[6] on the least-squares fits were applied to force exact agreement between the tabulated data and the approximations at $k=0$.

With the aerodynamic approximation of Eq. (3), the equations of motion given by Eq. (2) can be rewritten in state-space form as outlined in the Appendix. The resulting state-space model is then

$$\dot{x} = Fx + Gu \tag{4}$$

where x is the system state vector, F the system dynamics matrix, G the control input matrix, and u the control input vector containing the control surface deflections δ, control surface rates, and control surface accelerations, as defined in the Appendix. The eigenvalues of the system matrix F, where F is a function of q, are analyzed for system stability.

To validate the accuracy of the aerodynamic approximations and state-space models, a frequency-response analysis of the open-loop aircraft was performed. Vertical displacement responses of right-side forward-swept and aft-swept X-wing blade tips to a sinusoidal oscillation of the lower horizontal tail (Fig. 1) were calculated using the state-space model. These results were compared with frequency-response results obtained by substituting interpolated values of the tabulated GAF data directly into Eq. (2) in place of the approximated aerodynamics and setting $s=j\omega$. Comparisons of the results in Figs. 3 and 4 for both magnitude and phase show close agreement between results obtained with interpolated and approximated aerodynamics.

Dynamic Stability Analysis

The longitudinal and lateral dynamics state-space models of the flexible X-wing aircraft in the stopped-rotor mode were analyzed for static and dynamic stability by computing system eigenvalues for a range of flight conditions and plotting the results as a velocity root locus. These analyses were performed

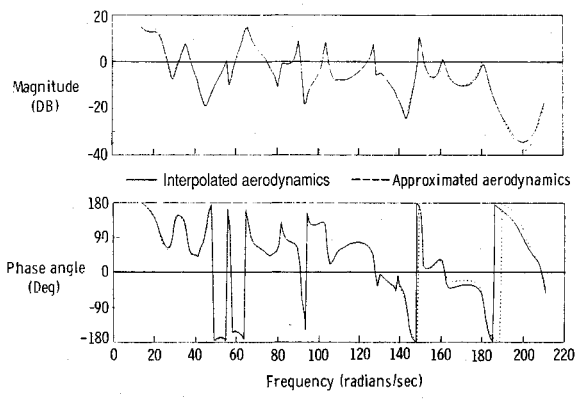

Fig. 3 Right-side forward blade-tip displacement response to lower horizontal stabilizer input ($V=200$ knots, sea level).

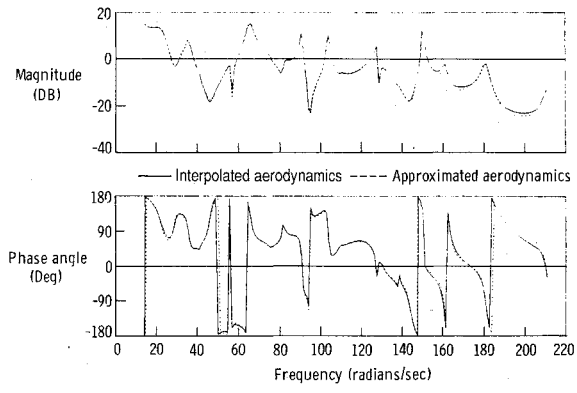

Fig. 4 Right-side aft blade-tip displacement response to lower horizontal stabilizer input ($V=200$ knots, sea level).

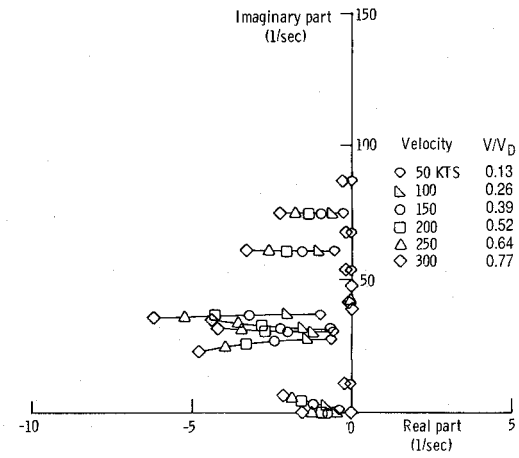

Fig. 5 Eigenvalue velocity root locus for lateral motion of flexible model at sea level.

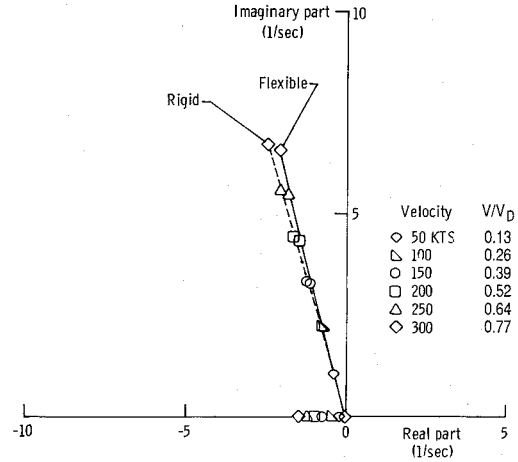

Fig. 6 Comparison of lateral-directional velocity root loci for rigid and flexible models at sea level.

to check for possible aeroelastic flutter, aeroelastic divergence, and possible body-freedom flutter, which is a coupling of rigid-body and flexible-body modes in an unstable flutter-like motion. The technique used leads to reliable predictions of instability speeds, depending on the quality of the aerodynamic approximation in the reduced-frequency range at which a mode crosses into the unstable right-half plane region.

Three series of analyses were performed, one each for the longitudinal and lateral dynamic models, and a third using a combined lateral/longitudinal model with a reduced set of symmetric and antisymmetric elastic vibration modes to check for possible coupling of the longitudinal and lateral dynamics. Two cases were run in both the lateral and longitudinal series, one using a model reduced to rigid-body modes only and the other using the complete set of rigid-body and elastic modes. The results of the third analysis series, which will not be shown, confirm that the longitudinal and lateral dynamics for the study configuration are uncoupled over the flight regime.

Lateral Stability

Eigenvalues of the system matrices of the rigid-body only and the full elastic model were computed for airspeeds from 50 to 300 knots at sea-level flight conditions using the ISAC computer code. The results are shown in the form of velocity root loci in Figs. 5 and 6. For comparison purposes, the airspeeds are also presented as a fraction of the hub-fixed divergence speed V_D. Figure 5 shows the full flexible model eigenvalue locations, with all of the eigenvalues in the (stable) left-half plane over the velocity range, including a spiral model eigenvalue near the origin, indicating that no aeroelastic antisymmetric flutter or divergence modes exist for this configuration. A comparison of the rigid-body analysis Dutch roll, spiral, and roll mode results with the full flexible model results for these modes is shown in Fig. 6. The only significant difference due to flexibility of the vehicle is a slight loss of Dutch roll damping at the higher velocities, with no visible change to the roll or spiral mode eigenvalues.

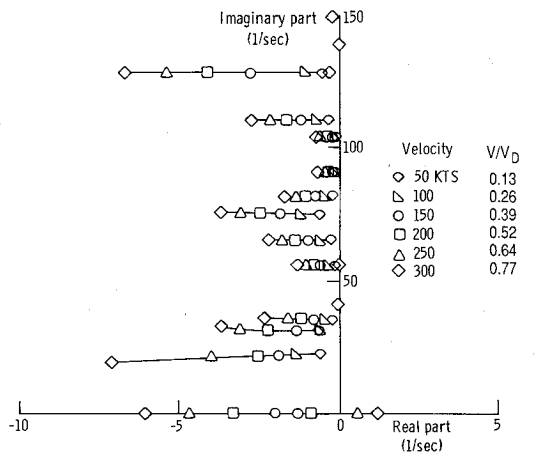

Fig. 7 Eigenvalue velocity root locus for longitudinal motion of flexible model at sea level.

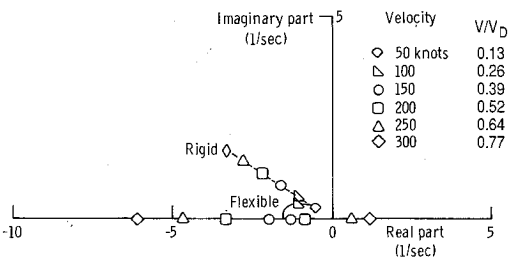

Fig. 8 Comparison of longitudinal velocity root loci for rigid and flexible models at sea level.

Longitudinal Stability

An analysis of the longitudinal dynamics of the X-wing aircraft similar to the lateral analysis described above was performed using both the rigid-body only and the full flexible models. The locus of system eigenvalues of the flexible model for the same 50- to 300-knot velocity range at sea level mentioned earlier is shown in Fig. 7. Again, the airspeeds are presented as a fraction of V_D. These results show that the high-frequency aeroelastic modes are all stable; however, there is a single eigenvalue that moves along the real axis into the unstable right-half plane, passing through the origin at 230 knots. This unstable eigenvalue is shown more clearly in Fig. 8, where the rigid-body only and flexible model short-period mode dynamics are compared. As shown, the rigid-body only model exhibits a classical short-period behavior with a complex conjugate eigenvalue pair increasing in frequency along a constant damping ratio line in the left-half plane. The flexible model results, on the other hand, show a different characteristic to the short-period mode eigenvalues, with the initially complex conjugate pair quickly becoming two roots on the real axis, with one root moving to the left and the other to the right into the unstable right-half plane at 230 knots.

The short-period root pattern of two real eigenvalues, although obviously due to the effects of structural flexibility in the present case, is characteristic of aircraft that are statically unstable. Therefore, the predicted instability is attributed to structural deformations causing a loss of aircraft static margin. This loss of static margin is consistent with static aeroelastic wash in of the forward-swept blades,[7] which is the tendency of the load on the blade to increase the local section geometric angle of attack, causing a further increase in the aerodynamic load. Aeroelastic wash in of forward-swept wings leads to forward shifts in aerodynamic center locations and can ultimately lead to structural divergence of the wing. Similarly, aft-swept blades undergo static aeroelastic wash out, which is the tendency of the load to result in a decrease in local section geometric angle of attack and thus limit the buildup of aerodynamic load due to deformation. Aeroelastic wash out of aft-swept wings also leads to forward shifts in aerodynamic center location. To verify that wash in and wash out were indeed the cause of the predicted instability, a static aeroelastic analysis method was formulated using a modal vibration approach to calculate static aeroelastic deformations and changes in static stability derivatives. Those results are described in the next section.

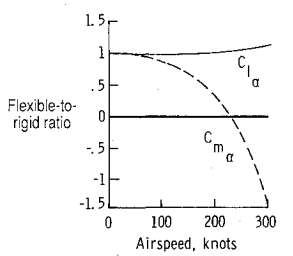

Fig. 9 Flexible-to-rigid ratios of C_{L_α} and C_{M_α} at sea level.

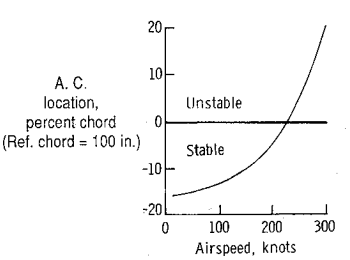

Fig. 10 Vehicle aerodynamic-center location relative to center of gravity at sea level.

Static Aeroelastic Analysis

The dynamic stability analyses described in the previous section were performed using first-order state-space mathematical models developed from the second-order matrix differential equations of motion of the vehicle, as given by Eq. (2). For steady-state conditions, the tabulated GAF data for $k=0$ can be substituted directly into Eq. (2) to obtain[8]

$$[K+qQ(k=0)]\xi+qQ_c(k=0)\delta=0 \tag{5}$$

Partitioning Eq. (5) according to rigid and flexible modes gives

$$\left[\begin{bmatrix}0&0\\0&K_{ff}\end{bmatrix}+q\begin{bmatrix}Q_{rr}&Q_{rf}\\Q_{fr}&Q_{ff}\end{bmatrix}\right]\begin{Bmatrix}\xi_r\\\xi_f\end{Bmatrix}+q\begin{bmatrix}Q_{rc}\\Q_{fc}\end{bmatrix}\delta=0 \tag{6}$$

where ξ_r is the partition of ξ corresponding to the lateral or longitudinal rigid-body mode displacements, and ξ_f the partition of ξ corresponding to the flexible-mode generalized coordinate deflections. Solving the second of the two equations (second row of the matrix equation) for ξ_f in terms of ξ_r and δ, results in

$$\xi_f=-(K_{ff}+qQ_{ff})^{-1}qQ_{fr}\xi_r-(K_{ff}+qQ_{ff})^{-1}qQ_{fc}\delta \tag{7}$$

Substituting for ξ_f in the first equation (first row of the matrix equation) gives the result

$$[Q_{rr}-qQ_{rf}(K_{ff}+qQ_{ff})^{-1}Q_{fr}]\xi_r + [Q_{rc}-qQ_{rf}(K_{ff}+qQ_{ff})^{-1}Q_{fc}]\delta=0 \tag{8}$$

The coefficients (square bracket terms) of the rigid-body motion ξ_r and control surface deflection δ in Eq. (8) consist of the aerodynamic forces due to the rigid-body shape (Q_{rr} and Q_{rc} matrices, respectively) and the additional aerodynamic forces due to static aeroelastic deformations. Dividing relevant elements of the coefficients of ξ_r and δ by the corresponding elements of the Q_{rr} and Q_{rc} matrices, respectively, gives the ratio of flexible-body to rigid-body aerodynamic force as a function of q. That is, the gain or loss of aerodynamic force due to structural deformation is given as a ratio, with a nearly rigid vehicle having flexible-to-rigid ratios near 1 for the entire q range of interest.

In the longitudinal direction, vertical translation z and pitch angle θ are the rigid-body mode displacements used in calculating unsteady GAF's and performing dynamic stability analyses. For steady state ($k=0$), the aerodynamic force and moment due to z displacement are zero, meaning that the columns of Q_{rr} and Q_{fr} associated with z are zero. Thus,

$$\xi_r=\begin{Bmatrix}z\\\theta\end{Bmatrix} \tag{9a}$$

$$Q_{rr}=\begin{bmatrix}0&L_\theta\\0&M_\theta\end{bmatrix} \tag{9b}$$

where L_θ is the lift due to pitch, and M_θ the moment due to pitch. For small perturbations of θ, these forces are the lift and moment due to angle of attack. When the total aerodynamic force is divided by the rigid-body aerodynamic force, the results are nondimensional flexible-to-rigid ratios of the aircraft lift-curve slope C_{L_α} and the static-stability derivative C_{M_α}.

Flexible-to-rigid ratios of C_{L_α} and C_{M_α} for the trimmed X-wing vehicle are shown in Fig. 9 for airspeeds up to 300 knots at sea-level flight conditions. The effects of flexibility on C_{L_α} are slight and concentrated at the higher flight speeds, with a ratio of 1.14 or a 14% increase in lift at 300 knots. The effect on C_{M_α} is much more pronounced, with the flexible-to-rigid ratio decreasing rapidly with increasing airspeed, passing through zero at 320 knots, and becoming of opposite sign, which corresponds directly to the passage of the real eigenvalue into the unstable region in Figs. 7 and 8.

The nearly constant C_{L_α} ratio and rapidly changing C_{M_α} ratio imply a redistribution or shift in center of aircraft lift rather than a change in total aircraft lift. Dividing C_{M_α} by C_{L_α} at every airspeed gives the aerodynamic center location relative to the vehicle center of gravity.[9] This result is shown in Fig. 10. The aerodynamic center at low airspeeds is aft of the center of gravity about 16 in., generating nose-down stabilizing pitching moments for positive angle-of-attack disturbances. As the airspeed increases, the aerodynamic center moves forward toward the center of gravity, reducing the nose-down pitching moment and therefore the stability of the aircraft. Above 230 knots, the aerodynamic center is forward of the center of gravity, generating unstable nose-up pitching moments due to positive angle-of-attack disturbances. This is the cause of the short-period instability shown in Fig. 8.

To investigate the wash in and wash out characteristics of the X-wing blades in this study, structural deformations of a forward- and aft-swept blade were calculated for a 1-deg angle-of-attack change of the vehicle for a range of flight velocities at sea level. Vertical blade displacements for this case are shown in Fig. 11. At the highest velocity, the forward-swept blade deflects upward at the tip about 1.7% of the blade length, which for this configuration is about 6-in. actual vertical displacement. The aft-swept blade deflects slightly

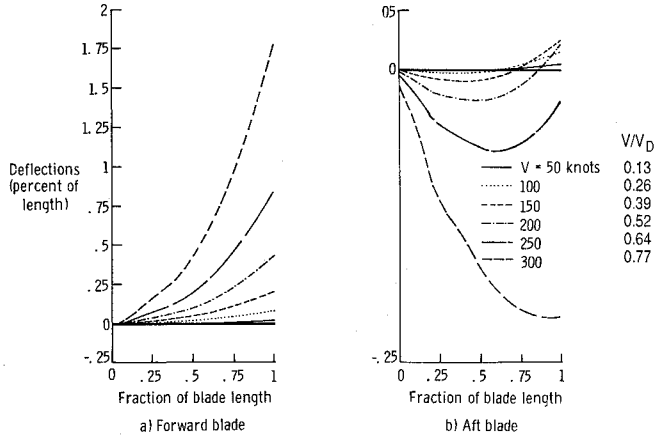

Fig. 11 Vertical static aeroelastic deflections of blades at sea level.

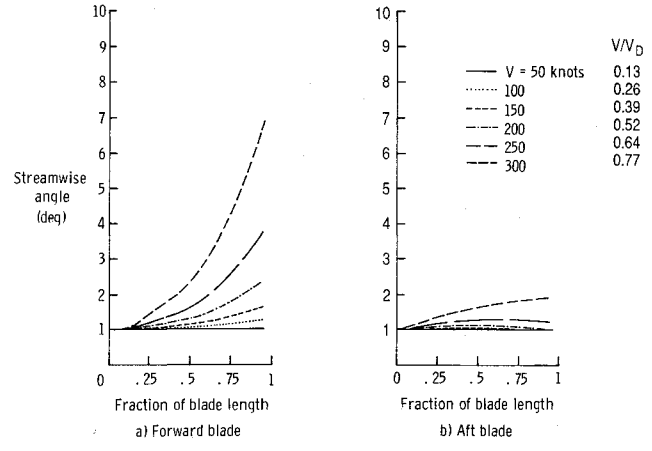

Fig. 12 Local section geometric angles of attack due to vertical blade deflection.

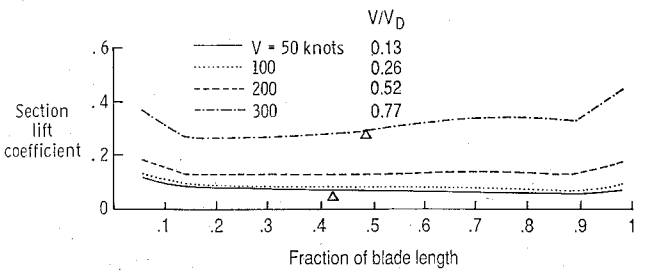

Fig. 13 Forward-blade left distribution and center locations at sea level.

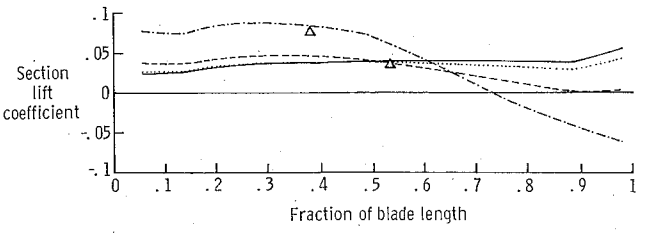

Fig. 14 Aft-blade lift distribution and center location at sea level.

downward about 0.2% of the blade length at the tip, or about 0.7-in. actual displacement at that same dynamic pressure. This downward deflection is apparently due to downwash effects of the forward blade inducing a net negative angle of attack on the aft-swept blade, contributing even more to a forward shift in aerodynamic center than that due just to aeroelastic wash out. Note, however, that the doublet-lattice aerodynamic theory used to predict these results assumes a flat, undeformed wake and therefore does not include the effects of deformations of the forward-swept blade wake over the aft-swept blade. These effects could be substantial and could either alleviate or further aggravate the shifts in aerodynamic center locations.

Plots of the local section geometric angle-of-attack changes due to static vertical deflection of the blades for the 1-deg aircraft angle-of-attack condition are shown in Fig. 12. The forward-swept blade shows increasing angles of attack due to vertical deflections (wash in) with a 6-deg increase at the tip for the highest dynamic pressure. For the aft-swept blade, the downward deflection results in an increase in local section geometric angle of attack along the span. This has the effect of reducing the negative lift being generated on the aft blade by downwash from the forward blade, thereby unloading the outboard sections of the aft blade.

Blade-lift distributions including static structural deformation for different flight speeds are shown in Figs. 13 and 14. Figure 13 shows an outboard (forward) shift in the center of the lift distribution with increased velocity. Figure 14 shows a reduction in outboard lift as velocity increases, corresponding to the aeroelastic wash out of the aft-swept blade. At 300 knots, the outboard third of the blade is actually carrying a down load, and the center of lift has shifted substantially inboard (forward).

Static aeroelastic deformations of stopped X-wing rotor system blades changing aircraft static margins and longitudinal stability and trim characteristics will probably be a generic problem for X-wing configuration aircraft. In the stopped-rotor mode, several of the X-wing rotor blades will have to be in a forward-swept position and will undergo aeroelastic wash in deformations. Furthermore, aeroelastic structural tailoring of composite structural material to force aeroelastic wash out of the forward-swept wing[10] will probably not be possible on X-wing rotor blades because of the requirements of rotary-wing flight and conversion for rotary-wing to fixed-wing flight modes. Control of the static aeroelastic blade deformations may well require the use of outboard control surfaces on the rotor blades or additional circulation-control blowing to varying degrees along the blade.

Conclusions

A static and dynamic aeroelastic stability analysis of an X-wing configuration aircraft including the aircraft flight dynamics (free-body) modes has been conducted. Lateral directional analysis results using antisymmetric aircraft vibration modes showed only a slight decrease in Dutch-roll mode damping due to X-wing blade flexibility effects. Longitudinal analysis results using symmetric vibration modes showed a dramatic change in aircraft short-period eigenvalues due to structural flexibility, leading to a unstable root pattern and a statically unstable aircraft.

A static aeroelastic analysis using a normal vibration mode approach was used to determine flexible-to-rigid ratios of the study configuration aircraft lift-curve slope, static stability derivative (moment-curve slope), and aerodynamic-center location relative to the aircraft center of gravity. These results showed that the aircraft aerodynamic center shifted forward with increasing speed, leading to the previously mentioned static instability. Analysis of the blade deformations showed that aeroelastic wash in of the forward-swept blades combined with downwash-induced down load on the aft-swept blade caused the aerodynamic center shift. Reductions in aircraft static margin and aircraft trim changes due to structural deformation will probably be generic problems of X-wing configuration aircraft and may require active blade deformation control for X-wing aircraft to achieve stable high-speed forward flight.

Appendix

The transformation of Eqs. (2) and (3) into state-space form along the lines of Ref. 3 is accomplsihed as follows. The matrices A_j and B_i in Eq. (3) are partitioned as

$$A_j = [A_j^\xi \mid A_j^c] \tag{A1a}$$

$$B_i = [B_i^\xi \mid B_i^c] \tag{A1b}$$

and the resulting expression for Eq. (3) is substituted into Eq. (2) to get

$$\left[Ms^2 + Cs + K + \sum_{i=1}^{L} w_i^\xi s\right]\xi + \left[qA_0^c + qA_1^c\left(\frac{bs}{V}\right) + qA_1^c\left(\frac{bs}{V}\right)^2 + \sum_{i=1}^{L} w_i^c s\right]\delta = 0 \tag{A2}$$

where

$$M = M + qA_2^\xi (b^2/V^2)$$

$$C = C + qA_1^\xi (b/V)$$

$$K = K + qA_0^\xi$$

$$w_i^\xi = (qB_i^\xi)/[s + (V/b)\beta_i]$$

$$w_i^c = (qB_i^c)/[s + (V/b)\beta_i]$$

Defining a vector x_i^a as

$$x_i^a = w_i^\xi s\xi + w_i^c s\delta = \frac{qs}{s + (V/b)\beta_i}[B_i^\xi \xi + B_i^c \delta] \tag{A3}$$

and expanding gives

$$sx_i^q = -\beta_i (V/b) I x_i^q + qsB_i^{\xi}\xi + qsB_i^{c}\delta \tag{A4}$$

which is a first-order equation for the aerodynamic lags associated with the unsteady GAF's. Defining a system state vector x and control input vector u as

$$x^T = \{\xi^T s\xi^T x_1^{q\,T} \ldots x_L^{q\,T}\} \tag{A5}$$

$$u^T = \{\delta^T s\delta^T s^2\delta^T\} \tag{A6}$$

Eqs. (A2) and (A4) can be combined as

$$sx = Fx + Gu \tag{A7}$$

or in the time domain

$$\dot{x} = Fx + Gu \tag{A8}$$

where the matrices F and G are

$$F = \begin{bmatrix} 0 & I & 0 & \ldots & 0 \\ -M^{-1}K & -M^{-1}C & -M^{-1} & \ldots & -M^{-1} \\ 0 & qB_1^{\xi} & -\beta_1 \dfrac{V}{b} I & 0 & \ldots \\ \vdots & \vdots & 0 & \cdot & \ldots \\ 0 & qB_L^{\xi} & \vdots & \ldots & -\beta_L \dfrac{V}{b} I \end{bmatrix} \tag{A9}$$

$$G = \begin{bmatrix} 0 & 0 & 0 \\ -M^{-1}A_0^c & -M^{-1}A_1^c \dfrac{b}{V} & -M^{-1}A_2^c \dfrac{b^2}{V^2} \\ 0 & B_1^c & 0 \\ \vdots & \vdots & \vdots \\ 0 & B_L^c & 0 \end{bmatrix} \tag{A10}$$

which is the same as Eq. (4).

References

[1] Haas, D. J. and Chopra, I., "Flutter of Circulation Control Wings," AIAA Paper 88-2345, April 1988.

[2] Lambert, M., "X-Wing Harrier Speed and Helicopter Hovering," *Interavia Review*, No. 5, 1985.

[3] Peele, E. L. and Adams, W. M., Jr., "A Digital Program for Calculating the Interaction Between Flexible Structures, Unsteady Aerodynamics, and Active Controls," NASA TM-80040, Jan. 1979.

[4] Mukhopadhyay, V., Newsom, J. R., and Abel, I., "A Method for Obtaining Reduced-Order Control Laws for High-Order Systems Using Optimization Techniques," NASA TP-1876, Aug. 1981.

[5] Tiffany, S. H. and Adams W. M., Jr., "Fitting Aerodynamic Forces in the Laplace Domain: An Application of a Nonlinear Nongradient Technique to Multilevel Constrained Optimization," NASA TM-86317, Oct. 1984.

[6] Abel, I., "An Analytical Technique for Predicting the Characteristics of a Flexible Wing Equipped With an Active Flutter-Suppression System and Comparison With Wind-Tunnel Data," NASA TP-1367, 1979.

[7] Bisplinghoff, R. L., Ashley, H., and Halfman, R. L., *Aeroelasticity*, Addison-Wesley Pub., Reading, MA, 1955, p. 483.

[8] Sheena, Z. and Karpel, M., "Static Aeroelastic Analysis Using Aircraft Vibration Modes," *Second International Symposium on Aeroelasticity and Structural Dynamics*, Aachen, West Germany, April 1985, pp. 229–232.

[9] Abel, I., "A Wind-Tunnel Evaluation of Analytical Techniques for Predicting Static Stability and Control Characteristics of Flexible Aircraft," NASA TN D-6656, Mrch 1972.

[10] Weisshaar, T. A., "Aeroelastic Tailoring of Forward Swept Composite Wings," *Journal of Aircraft*, Vol. 18, Aug. 1981, pp. 669–676.